crystals

MDPI

Article

Analysis and Optimization of the Machining Characteristics of High-Volume Content SiCp/Al Composite in Wire Electrical Discharge Machining

Hongzhi Yan, Bakadiasa Djo Kabongo, Hongbing Zhou, Cheng Wu and Zhi Chen *

State Key Laboratory of High Performance Complex Manufacturing, College of Mechanical and Electrical Engineering, Central South University, Changsha 410083, China; hongzhiyan1964@gmail.com (H.Y.); djokabongo@163.com (B.D.K.); zhouhongbing196@gmail.com (H.Z.); w18358838436@163.com (C.W.)
* Correspondence: jdydqb@csu.edu.cn; Tel.: +86-18202764498

Abstract: With the properties of high specific strength, small thermal expansion and good abrasive resistance, the particle-reinforced aluminum matrix composite is widely used in the fields of aerospace, automobile and electronic communications, etc. However, the cutting performance of the particle-reinforced aluminum matrix composite is very poor due to severe tool wear and low machining efficiency. Wire electrical discharge machining has been proven to be a good machining method for conductive material with any hardness. Even so, the high-volume SiCp/Al content composite is still a difficult-to-machine material in wire electrical discharge machining due to the influence of insulative the SiC particle. The goal of this paper is to analyze the machining characteristics and find the optimal process parameters for the high-volume content (65 vol.%) SiCp/Al composite in wire electrical discharge machining. Experimental results show that the material removal method of the SiCp/Al composite includes sublimating, decomposing and particle shedding. The material removal rate is found to increase with the increasing pulse-on time, first increasing and then decreasing with the increasing pulse-off time, servo voltage, wire feed and wire tension. Pulse-on time and servo voltage are the dominant factors for surface roughness. In addition, the multi-objective optimization method of the nondominated neighbor immune algorithm is presented to optimize the process parameters for a fast material removal rate and low surface roughness. The optimized process parameters can increase the material removal rate by 34% and reduce the surface roughness by 6%. Furthermore, the effectiveness of the Pareto optimal solution is proven by the verified experiment.

Keywords: wire electrical discharge machining; SiCp/Al composite; process parameters optimization; nondominated neighbor immune algorithm

Citation: Yan, H.; Kabongo, B.D.; Zhou, H.; Wu, C.; Chen, Z. Analysis and Optimization of the Machining Characteristics of High-Volume Content SiCp/Al Composite in Wire Electrical Discharge Machining. *Crystals* **2021**, *11*, 1342. https://doi.org/10.3390/cryst11111342

Academic Editor: Pavel Lukáč

Received: 21 October 2021
Accepted: 31 October 2021
Published: 3 November 2021

1. Introduction

The particle-reinforced aluminum matrix composite is a material that is prepared by adding reinforcement to the aluminum matrix, such as carbide, nitride or graphite. Compared with the aluminum matrix, the particle-reinforced aluminum matrix composite has better physical and chemical properties, such as low density, high specific strength, excellent high-temperature properties, high wear resistance and excellent stability dimensional [1–3]. The SiCp/Al composite is one of the most common particle-reinforced aluminum matrix composites, which is widely used in the fields of aerospace, automobiles and electronic communications, etc. Due to the non-uniform distribution of super-hard SiC particles, SiCp/Al is a difficult-to-machine material in the traditional cutting method. The major displays of machining difficulties are severe tool wear, low machining efficiency and surface defects [4]. With an increasing volume content of the SiC particle, the machining process becomes more and more difficult. This fact severely limits the application and extension of the particle-reinforced aluminum matrix composite.

In wire electrical discharge machining (EDM/WEDM), a good deal of pulse sparks occurs between the electrode and the workpiece. Every pulse spark can produce a small

discharge crater (diameter of 1–100 μm) due to melting or vaporizing from high-density thermal energy (1–10 × 10^6 J/m^2) [5,6]. Then, continuous pulse sparks can cause considerable material removal efficiency. Because the maximum instantaneous temperature between the electrode and the workpiece can be up to 10,000 °C, EDM/WEDM can process various conductive materials regardless of hardness [7–9]. Hence, EDM/WEDM is an alternative method for SiCp/Al composites.

In recent years, much research has been carried out to investigate the machining characteristics of the particle-reinforced aluminum matrix composite in EDM/WEDM. Balasubramaniam V. et al. [10], Gu L. [11], Dey A. [12], Daneshmand S. [13] and Shelvaraj S.G. et al. [14] analyzed the effects of process parameters on the material removal rate (*MRR*), surface roughness (*SR*) and electrode wear rate (*TWR*) in EDM of aluminum matrix composites with a particle content of 7.5–20%. It was pointed out that the method of process parameter optimization could evidently improve the machining characteristics. Singh B [15] compared *TWR* in traditional EDM and powder-mixed EDM of aluminum matrix composites with a particle content of 10%. It was found that tungsten powder could effectively reduce *TWR*. Pramanik A [16] studied the effect of wire tension and discharge current on the *MRR* and surface quality in WEDM of aluminum matrix composites with a particle content of 10%. It was pointed out that surface roughness first decreased and then increased with an increasing discharge current. Kumar N.M. et al. [17] investigated the influence of particle content on the machining characteristics of aluminum matrix composites with particle contents of 0–8% in EDM. It was pointed out that the performance of EDM decreased with an increasing particle content. Bains P.S. [18] employed the magnetic field method to improve surface properties of aluminum matrix composites with a particle content of 37–50% in EDM. It was pointed out that this method could significantly reduce surface microhardness and the thickness of the recast layer. Kumar T.T.S. et al. [19] adopted a response surface methodology to determine the optimal process parameters for aluminum matrix composites with a particle content of 20% in WEDM. Uthayakumar M. [20] analyzed the effects of process parameters on the machining speed and surface roughness of aluminum hybrid composites with a particle content of 20% in EDM. Besides, the gray relational analysis method was adopted to obtain the optimal process parameters for aluminum hybrid composites. Senthilkumar T.S. [21] investigated the effect of particle content on the surface topography in EDM of aluminum hybrid composites with a particle content of 5–8%. It was found that, with an increase in particle content, *MRR* decreased, while the surface hardness and the diameter of the craters increased. Paswan K. et al. [22] utilized steam as a dielectric medium for machining metal matrix composites with a particle content of 10% in EDM. Compared with the traditional kerosene medium, steam could significantly improve machining efficiency, surface quality and economic benefit. Devi M.B. et al. [23] completed an experimental study to determine the optimal process parameters for aluminum hybrid composites with a particle content of 6% in EDM. It was pointed out that the optimal process parameters for aluminum hybrid composites changed with the content of the reinforced particle.

From abovementioned research, we can find that EDM/WEDM has been proven to be a good machining method for particle-reinforced aluminum matrix composites. Besides, the process parameters are key factors for the machining characteristics of particle-reinforced aluminum matrix composites. However, the particle contents of aluminum matrix composites in the abovementioned research are relatively low. As pointed out in reference [17], with an increasing of particle content, the aluminum matrix composite becomes more and more difficult to machine. The optimal process parameters for aluminum matrix composites with different particle contents are also different.

The research object of this paper is the aluminum matrix composite with a high-volume content of reinforced particles (65 vol.% SiCp/Al composite). A set of discharge cutting experiments is carried out to investigate the effects of process parameters on the *MRR* and *SR* of the SiCp/Al composite. The machining mechanism of the SiCp/Al composite is revealed through a scanning electron microscope (SEM). In addition, the multi-

objective optimization method of the nondominated neighbor immune algorithm (NNIA) is presented to optimize the process parameters for fast *MRR* and low *SR*. The feasibility and precision of the optimal process parameters are evaluated by a verified experiment.

2. Materials and Methods

2.1. Material

The mechanical and physical properties of the 65 vol.% SiCp/Al composite are excellent, such as high thermal conductivity, high specific strength and good abrasive resistance. The specific stiffness of the 65 vol.% SiCp/Al composite is three times higher than the aluminum matrix and 25 times higher than copper. This material is praised as a third-generation electronic packaging material, which is widely used in civil electronic equipment, IGBT plate substrates and wireless base stations. The 65 vol.% SiCp/Al composite in this study is from Xi'An Fadi Technology Co., Ltd. (Xi'An, China) The material properties of the 65 vol.% SiCp/Al composite are listed in Table 1. In addition, the material properties of the SiCp/Al composite can be obtained according to the theory in Ref. [24]. The geometric dimension of the SiCp/Al composite basal plate is 150 mm × 50 mm × 4 mm.

Table 1. The material properties of 65 vol.% SiCp/Al composite.

Properties	Value
Thermal conductivity	180 W/mK
Thermal expansivity	7.42 ppm/K
Young modulus	230 GPa
Shear modulus	75 GPa
Flexure strength	350 MPa
Density	2.96 g/cm^3
Reinforced particle size	5–50 μm

2.2. Machine Tools

All discharge cutting experiments are carried out on a wire EDM machine (ACCUTX EZ-43 SA) from ACCUTEX technologies Co., Ltd. (Taiwan, China), as shown in Figure 1. It mainly consists of a workbench, a motion platform, a wire-moving system, a cooling system, CNC and a high-frequency pulse electrical source (the peak discharge voltage is 80 V). The dielectric is deionized water. The wire electrode is copper wire with a diameter of 0.25 mm. The workpiece is completely submerged in deionized water during the discharge process.

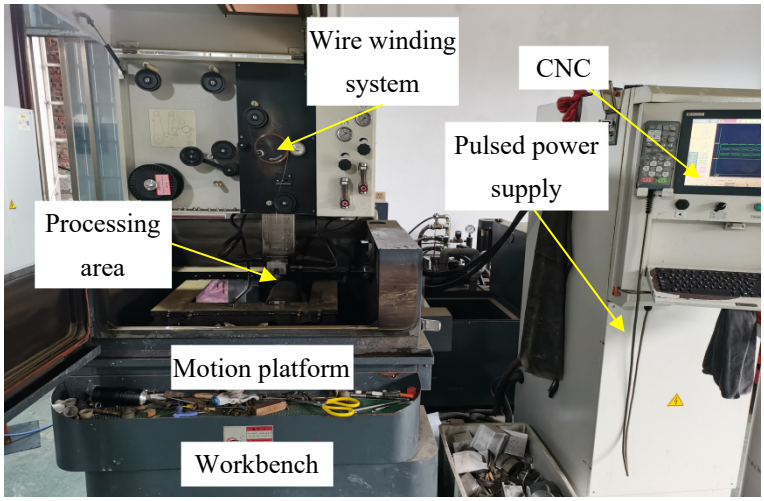

Figure 1. ACCUTEX EZ-43 SA machine tool.

2.3. The Experiment Design

A set of discharge cutting experiments is implemented to investigate the effects of process parameters on machining characteristics of the 65 vol.% SiCp/Al composite. Consequently, five important process parameters are selected as input factors, which include the pulse-on time (T_{on}), pulse-off time (T_{off}), servo voltage (SV), wire feed (WF) and wire tension (WT). Each process parameter has five levels, as shown in Table 2. Besides this, the material removal rate (MRR) and surface roughness (SR) are chosen as output factors. The calculating formula of MRR is as shown in Equation (1). The arithmetical mean deviation of the profile (Ra) is selected to represent the surface roughness (SR), which is measured by an optical profilometer (WYKO NT9100). The mean value of three measured data is treated as the final value of Ra. The design of discharge cutting experiments is as shown in Table 3. In this study, the discharge current is a constant value, because the machining efficiency is too slow if the discharge current is lower than 10 A, and frequent wire breakages will happen if the discharge current is higher than 10 A.

$$MRR = \frac{HL}{t} \tag{1}$$

Here, H is the thickness of the workpiece (mm), L is the cutting length (mm) and t is the cutting time recorded by a stopwatch. The cutting length is set as 10 mm.

The machined surface of the SiCp/Al composite is characterized by a scanning electron microscope (SEM, MIRA 3 LMU) under an acceleration voltage of 20.0 kV and magnification of 1000×.

Table 2. Process parameters and their levels.

Parameters	Unit	Level				
T_{on}	ns	250	300	350	400	450
T_{on}	μs	8	9	10	11	12
SV	V	41	43	45	47	49
WF	mm/s	8	9	10	11	12
WT	N	10	11	12	13	14

Table 3. The design of discharge cutting experiments.

No.	T_{on} (ns)	T_{off} (μs)	SV (V)	WF (mm/s)	WT (N)
1	250	10	45	10	12
2	300	10	45	10	12
3	350	10	45	10	12
4	400	10	45	10	12
5	450	10	45	10	12
6	350	8	45	10	12
7	350	9	45	10	12
8	350	11	45	10	12
9	350	12	45	10	12
10	350	10	41	10	12
11	350	10	43	10	12
12	350	10	47	10	12
13	350	10	49	10	12
14	350	10	45	8	12
15	350	10	45	9	12
16	350	10	45	11	12
17	350	10	45	12	12
18	350	10	45	10	10
19	350	10	45	10	11
20	350	10	45	10	13
21	350	10	45	10	14

3. Experiment Results and Discussion

3.1. Experiment Result

On the basis of the design of discharge cutting experiments, the results of discharge cutting experiments can be obtained, as shown in Table 4. The relative deviation of surface roughness is about 0.1–0.5 μm due to the instrumental error and different measure position.

Table 4. The results of discharge cutting experiments.

No.	T_{on} (ns)	T_{off} (μs)	*SV* (V)	*WF* (mm/s)	*WT* (N)	*MRR* (mm^2/s)	*SR* (μm)
1	250	10	45	10	12	0.265	4.42 ± 0.32
2	300	10	45	10	12	0.296	4.78 ± 0.25
3	350	10	45	10	12	0.404	4.86 ± 0.16
4	400	10	45	10	12	0.417	5.01 ± 0.28
5	450	10	45	10	12	0.465	5.16 ± 0.19
6	350	8	45	10	12	0.374	4.78 ± 0.1
7	350	9	45	10	12	0.392	4.86 ± 0.45
8	350	11	45	10	12	0.320	4.7 ± 0.36
9	350	12	45	10	12	0.315	4.77 ± 0.31
10	350	10	41	10	12	0.408	4.83 ± 0.5
11	350	10	43	10	12	0.430	4.97 ± 0.41
12	350	10	47	10	12	0.333	4.52 ± 0.38
13	350	10	49	10	12	0.308	4.69 ± 0.16
14	350	10	45	8	12	0.364	4.89 ± 0.25
15	350	10	45	9	12	0.354	4.71 ± 0.19
16	350	10	45	11	12	0.364	4.81 ± 0.26
17	350	10	45	12	12	0.351	4.88 ± 0.38
18	350	10	45	10	10	0.348	4.59 ± 0.45
19	350	10	45	10	11	0.360	4.82 ± 0.26
20	350	10	45	10	13	0.354	4.88 ± 0.29
21	350	10	45	10	14	0.364	4.77 ± 0.22

3.2. Machined Surface Characteristics

Figure 2 shows the machined surface of the SiCp/Al composite characterized by SEM. Combined with the XRD results of our previous research [25], a large quantity of microspheres is found on the machined surface. This is because the aluminum matrix can be sublimated under an ultrahigh temperature field (up to 10,000 °C) [8,26–29] due to discharge sparks. The sublimated aluminum matrix can become solid due to the cooling effect of the dielectric during the pulse-off time. Then, this material can adhere to the machined surface again in the form of a sphere. Besides, many microspheres can accumulate and form a blocky solid metal with many tentacles. This solid metal is called the recast layer. In addition, a large number of micropores are found on the machined surface. A part of the micropores is produced as a result of the gas entering the sublimated aluminum matrix during the recrystallizing process [30]. The other part of the micropores is produced in the preparation process of the SiCp/Al composite. Moreover, microcracks are found on the machined surface. This is the result of the non-uniform temperature field and rapid cooling [31]. Furthermore, many SiC particles and SiC shedding pits are found on the machined surface. As we know, the decomposition point of the SiC particle is higher than the boiling point of the aluminum matrix. Then, it is difficult to remove the SiC particle. When a part of the aluminum matrix around the SiC particle is sublimated, this SiC particle will be exposed. When the aluminum matrix around the SiC particle is completely sublimated, this SiC particle will be shed. Then, the shedding pits will be formed. This is consistent with the perspective in Ref. [32]. In addition, the influence of the direct sublimating of the aluminum matrix from a solid to a gas (thermal dissociation), the thermochemical interaction between ions and the deposition of more-complex secondary compounds of the second order may also contribute to the method of removal of SiCp/Al in EDM/WEDM [33].

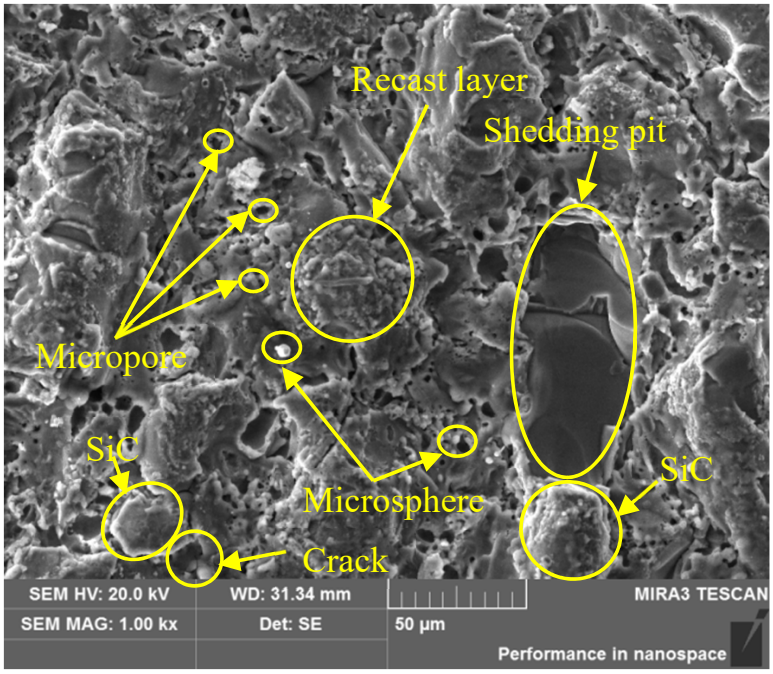

(**a**)

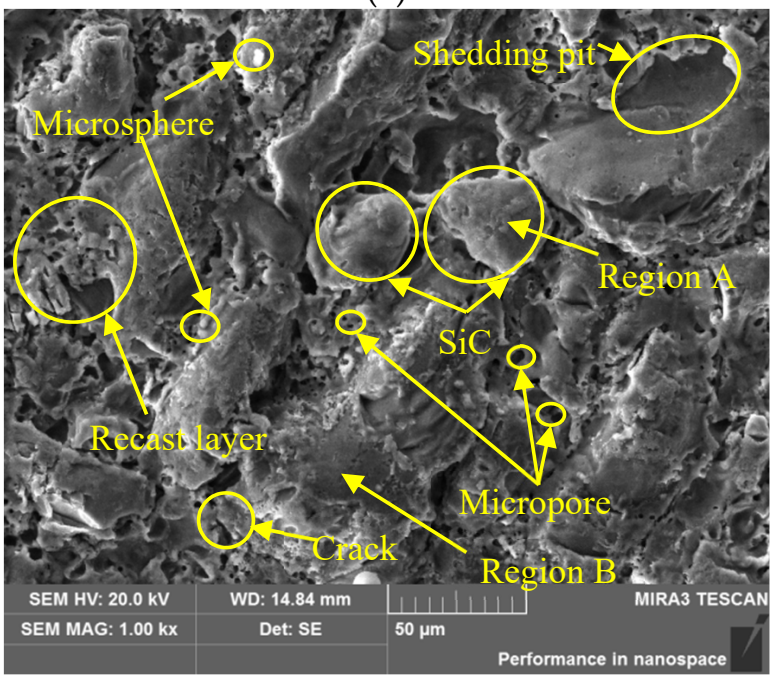

(**b**)

Figure 2. SEM micrographs of the machined surface of SiCp/Al composite. (**a**) No. 1 in Table 4. (**b**) No.4 in Table 4.

Figure 3 shows the results of EDS measurement on the machined surface of No.4 in Table 4. Table 5 shows the element composition on the machined surface of No.4 in Table 4. In region A, the contents of C, Si and O elements are obviously higher than those of other elements. Besides, in region B, the contents of C, Al and O elements are obviously higher than those of other elements. Hence, it can be inferred the main material in region A and region B are SiC particle and Al substrate, respectively. Moreover, the existence of O element means the redox reaction occurs during the machining process. The Cu element on the machined surface is transferred from the wire electrode due to the violent collision

between electron and ion. In addition, in region A, the volume content of the Si element is significantly lower than that of the C element. This may have resulted from the thermal decomposition of the SiC particle.

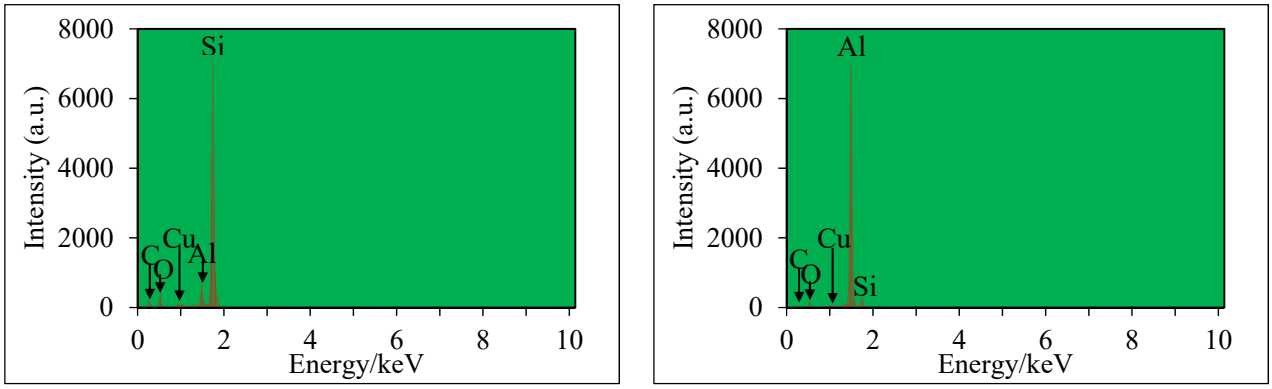

Figure 3. The results of EDS measurement on the machined surface of No.4 in Table 4. (**a**) Region A. (**b**) Region B.

Table 5. The element composition on the machined surface of No.4 in Table 4.

Element	Region A		Region B	
	Weight%	Atomic%	Weight%	Atomic%
C	31.05	46.79	18.90	32.41
O	18.31	20.72	11.23	14.47
Al	3.36	2.25	63.19	48.24
Si	46.66	30.07	6.63	4.86
Cu	0.61	0.17	0.05	0.01
Totals	100.00	100.00	100.00	100.00

3.3. The Effects of Process Parameters on MRR and SR

According to Table 4, the effects of process parameters on *MRR* and *SR* can be acquired, as shown in Figures 4–8. The degree of influence for *MRR* from high to low in order is T_{on}, *SV*, *Toff*, *WS* and *WF*. T_{on} and *SV* are the dominant factors for surface roughness (*SR*). The other three process parameters have a small effect on *SR*.

Figure 4 shows the effect of T_{on} on *MRR* and *SR*. *MRR* and *SR* are found to increase with the increase in T_{on}. The growth rate of *MRR* decreases with the increase in T_{on}. This is because a longer T_{on} can produce larger discharge energy in the single-pulse discharge process. Then, more material can be sublimated and decomposed, which can result in a fast machining speed. A larger discharge crater can be formed, which can lead to a rougher workpiece surface. In addition, the discharge debris between the wire electrode and the workpiece will be greater and greater corresponding to T_{on}. The probability of an arc discharge or short circuit will increase alongside T_{on}, which is harmful to the material removal. Hence, with the increasing of T_{on}, the growth rate of *MRR* becomes slower and slower.

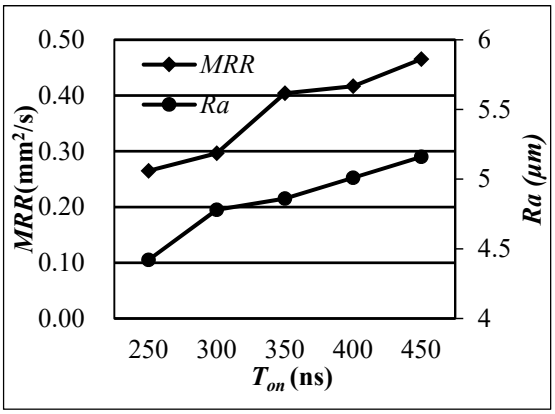

Figure 4. The effect of T_{on} on *MRR* and *SR*.

Figure 5 shows the effect of T_{off} on *MRR* and *SR*. *MRR* is found to first increase and then decrease with an increasing T_{off}. On the one hand, an increasing pulse-off time means there is more time to flush the sublimated and decomposed material, which is beneficial to the material removal. On the other hand, a longer T_{off} can lead to a smaller discharge energy produced in the continuous discharge process. Then, less material can be sublimated and decomposed, which can result in a slow machining speed. In addition, T_{off} has a small effect on *SR*. This is because shedding is one form of material removal of the SiCp/Al composite. The shedding pit is a key factor affecting *SR*. The geometric dimensioning of the shedding pit is decided by the size of the SiC particle.

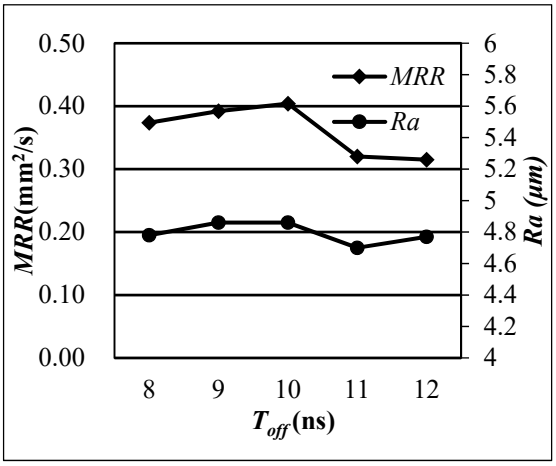

Figure 5. The effect of T_{off} on *MRR* and *SR*.

Figure 6 shows the effect of *SV* on *MRR* and *SR*. *MRR* is found to first increase and then decrease with an increasing *SV*. This is because increasing *SV* means increasing the discharge energy for removing the material, which is beneficial to material removal. It will result in the wire frequently drawing back if *SV* exceeds the critical value, which is harmful to material removal [26]. *SR* is found to first increase and then decrease with an increasing *SV*. This is because, on the one hand, an increasing *SV* can increase the discharge energy in the single-pulse discharge process, which can result in a rough workpiece surface. On the one hand, increasing *SV* can increase the discharge gap between the wire electrode and the workpiece. Then, more discharge debris can be expelled, which can lead to a smoother workpiece surface.

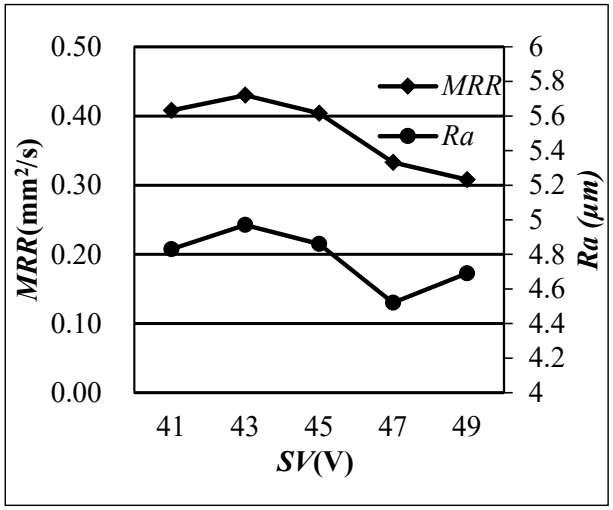

Figure 6. The effect of *SV* on *MRR* and *SR*.

Figure 7 shows the effect of *WF* on *MRR* and *SR*. *MRR* is found to first increase and then decrease with an increasing *WF*. When *WF* is relatively low, increasing *WF* can enhance the flow of the dielectric, which is beneficial to the discharge debris being expelled. When *WF* exceeds the critical value, increasing the *WF* can result in obvious wire vibration, which is harmful to the stability of the discharge process. In addition, *WF* does not have a significant effect on *SR*.

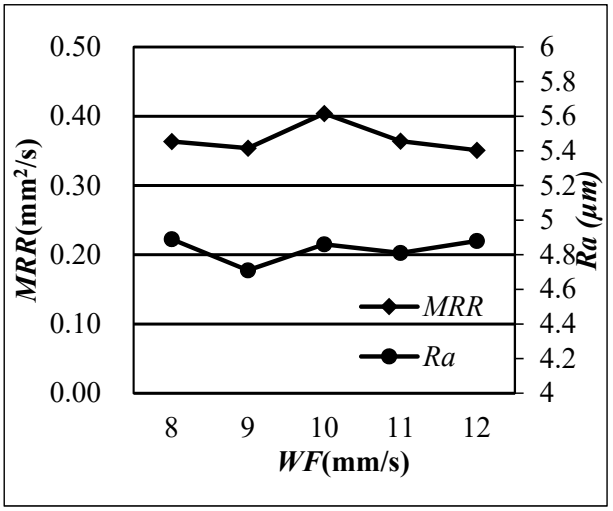

Figure 7. The effect of *WF* on *MRR* and *SR*.

Figure 8 shows the effect of *WT* on *MRR* and *SR*. *MRR* is found to first increase and then decrease with an increasing *WT*. When *WT* is relatively low, increasing *WF* can reduce the deflection of the wire electrode, which is beneficial to the discharge debris being expelled. When *WT* exceeds the critical value, increasing *WF* can result in wire electrode plastic deformation so as to enhance the wire vibration, which is harmful to the stability of the discharge process. In addition, *WT* does not have a significant effect on *SR*.

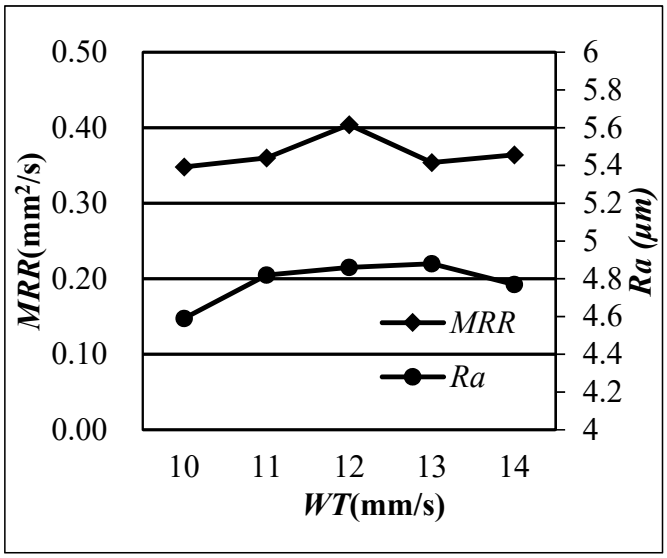

Figure 8. The effect of *WT* on *MRR* and *SR*.

3.4. The Numerical Relationship between Process Parameters on MRR/SR

Based on the experimental data in Table 4, the numerical relationship between process parameters on *MRR*/*SR* can be obtained through the method of nonlinear regression fitting, as shown in Equations (2) and (3). The numerical analysis software of Minitab was used to obtain the nonlinear regression fitting equation. The nonlinear regression algorithm is Gauss–Newton regression, whereby the maximum number of iterations is 200 and the convergence tolerance is 0.00001. Figures 9 and 10 show the residual plots for *MRR* and *SR*, respectively. The fitting residuals of *MRR* and *SR* essentially obey a normal distribution. In addition, Table 6 shows the comparative results of experimental data and fitting data. The relative errors between experimental data and fitting data are less than ±8%. The obtained nonlinear regression fitting equations of *MRR* and *SR* can be used to optimize the multi-objective process parameters.

$$\begin{aligned}\frac{MRR}{MRR^0} &= -2.0396 + 0.001618 \times \frac{T_{on}}{T_{on}^0} - 8.23419 \times 10^{-7} \times \frac{T_{on}}{T_{on}^0} \times \frac{T_{on}}{T_{on}^0} + 0.11923 \times \frac{T_{off}}{T_{off}^0} \\ &-0.00691149 \times \frac{T_{off}}{T_{off}^0} \times \frac{T_{off}}{T_{off}^0} + 0.0354379 \times \frac{SV}{SV^0} - 0.000558755 \times \frac{SV}{SV^0} \times \frac{SV}{SV^0} \\ &+0.0719239 \times \frac{WF}{WF^0} - 0.00367 \times \frac{WF}{WF^0} \times \frac{WF}{WF^0} + 0.102123 \times \frac{WT}{WT^0} \\ &-0.00414678 \times \frac{WT}{WT^0} \times \frac{WT}{WT^0}\end{aligned} \quad (2)$$

$$\begin{aligned}\frac{SR}{SR^0} &= -9.89602 + 0.004361 \times \frac{T_{on}}{T_{on}^0} - 1.34469 \times 10^{-6} \times \frac{T_{on}}{T_{on}^0} \times \frac{T_{on}}{T_{on}^0} + 0.255117 \times \frac{T_{off}}{T_{off}^0} \\ &-0.0136559 \times \frac{T_{off}}{T_{off}^0} \times \frac{T_{off}}{T_{off}^0} + 0.396492 \times \frac{SV}{SV^0} - 0.00481102 \times \frac{SV}{SV^0} \times \frac{SV}{SV^0} \\ &-0.213001 \times \frac{WF}{WF^0} + 0.01105 \times \frac{WF}{WF^0} \times \frac{WF}{WF^0} + 0.807388 \times \frac{WT}{WT^0} \\ &-0.03189 \times \frac{WT}{WT^0} \times \frac{WT}{WT^0}\end{aligned} \quad (3)$$

where T_{on}^0 is 1 ns, T_{off}^0 is 1 μs, SV^0 is 1 V, WF^0 is mm/s, WT^0 is 1 N, MRR^0 is 1 mm^2/s and SR^0 is 1 μm. The units of *MRR* and *Ra* are mm^2/s and μm, respectively.

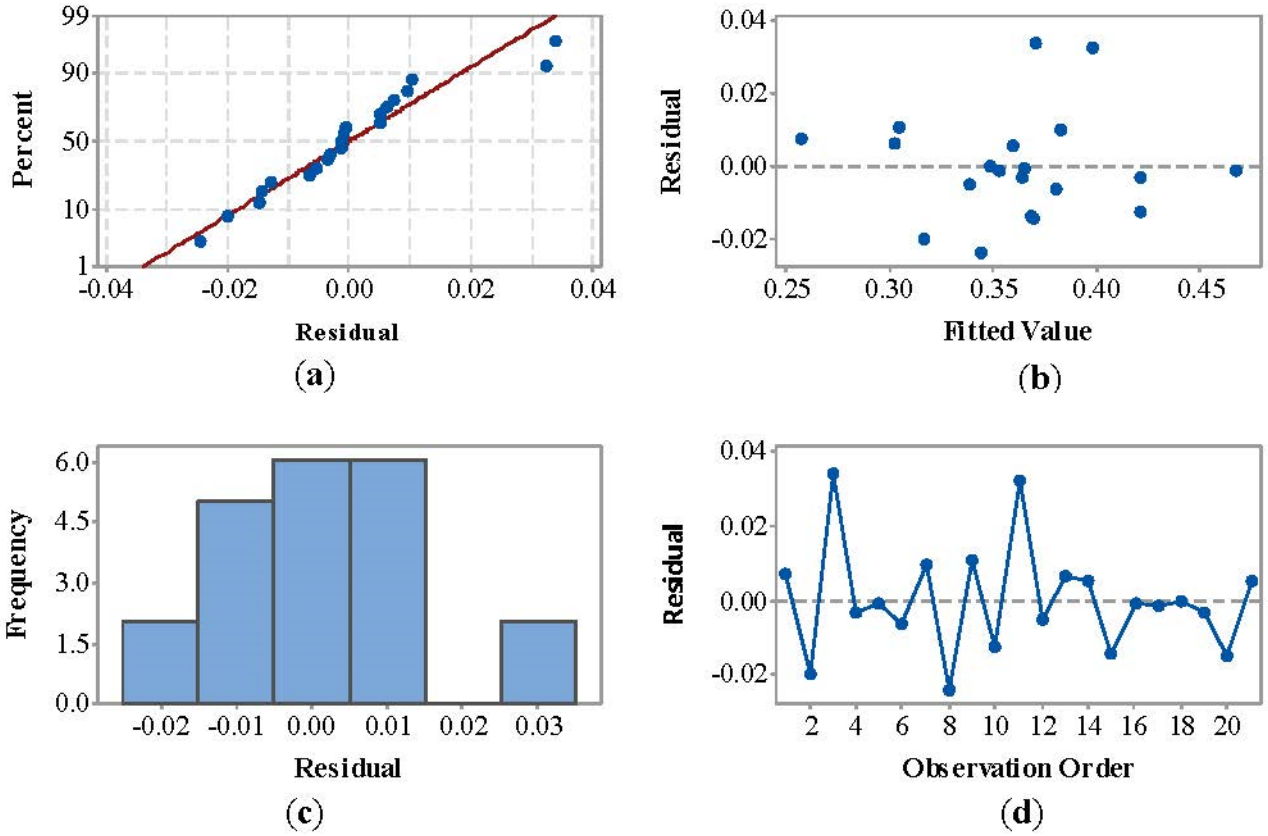

Figure 9. Residual plots for *MRR* (mm^2/s). (**a**) Normal Probability plot. (**b**) Versus Fits. (**c**) Histogram. (**d**) Versus Order.

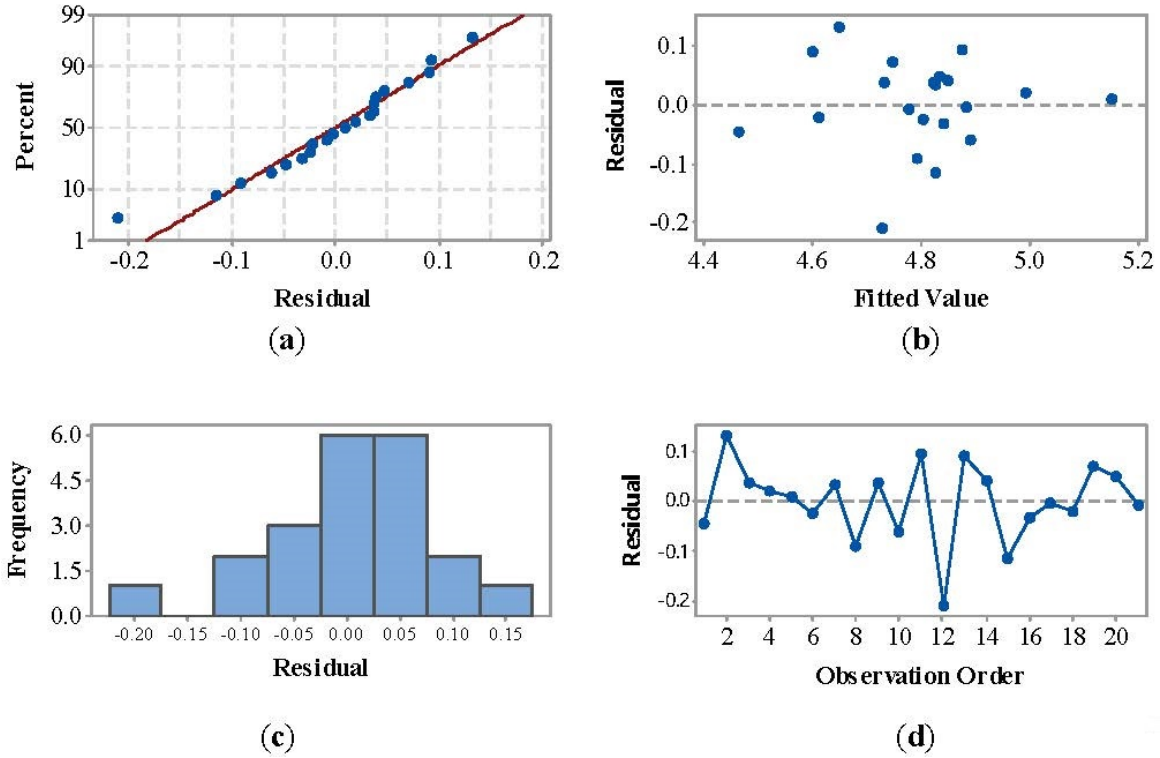

Figure 10. Residual plots for *SR* (μm). (**a**) Normal Probability plot. (**b**) Versus Fits. (**c**) Histogram. (**d**) Versus Order.

Table 6. The comparative results of experimental data and fitting data.

No.	T_{on} (ns)	T_{off} (μs)	*SV* (V)	*WF* (mm/s)	*WT* (N)	*MRR* (mm²/s)			*SR* (μm)		
						Exp.	Fit.	Re. (%)	Exp.	Fit.	Re. (%)
1	250	10	45	10	12	0.265	0.258	−2.69	4.42	4.47	1.06
2	300	10	45	10	12	0.296	0.316	6.81	4.78	4.65	−2.76
3	350	10	45	10	12	0.404	0.370	−8.34	4.86	4.82	−0.77
4	400	10	45	10	12	0.417	0.420	0.80	5.01	4.99	−0.40
5	450	10	45	10	12	0.465	0.466	0.27	5.16	5.15	−0.17
6	350	8	45	10	12	0.374	0.381	1.78	4.78	4.80	0.50
7	350	9	45	10	12	0.392	0.382	−2.45	4.86	4.83	−0.68
8	350	11	45	10	12	0.320	0.344	7.62	4.7	4.79	1.93
9	350	12	45	10	12	0.315	0.305	−3.28	4.77	4.73	−0.80
10	350	10	41	10	12	0.408	0.421	3.13	4.83	4.89	1.27
11	350	10	43	10	12	0.430	0.398	−7.50	4.97	4.88	−1.89
12	350	10	47	10	12	0.333	0.338	1.61	4.52	4.73	4.65
13	350	10	49	10	12	0.308	0.302	−1.96	4.69	4.60	−1.93
14	350	10	45	8	12	0.364	0.359	−1.43	4.89	4.85	−0.80
15	350	10	45	9	12	0.354	0.368	4.02	4.71	4.83	2.45
16	350	10	45	11	12	0.364	0.365	0.28	4.81	4.84	0.65
17	350	10	45	12	12	0.351	0.352	0.40	4.88	4.88	0.05
18	350	10	45	10	10	0.348	0.349	0.15	4.59	4.61	0.45
19	350	10	45	10	11	0.360	0.364	0.99	4.82	4.75	−1.48
20	350	10	45	10	13	0.354	0.369	4.17	4.88	4.83	−0.97
21	350	10	45	10	14	0.364	0.359	−1.40	4.77	4.78	0.19

Exp.: Experimental data, Fit.: Fitting data, Re.: Relative error.

4. Process Parameters Optimization

4.1. NNIA

As pointed out in Section 3.3, the effect degree and impact trend of process parameters on *MRR* and *SR* are different. In the practical machining process, it is desired that the workpiece is quickly removed with low surface roughness. Hence, the method of multi-objective process parameter optimization is suitable for the above issue.

In this study, the multi-objective optimization method of the nondominated neighbor immune algorithm is presented to optimize the process parameters for fast *MRR* and low *SR*. NNIA is a multi-objective optimization algorithm, which simulates the natural immune function. This algorithm is inspired by immunology, which simulates the phenomena of the commensalism of various antibodies and the activation of a small number of antibodies during the immunologic process. This small number of relatively independent nondominated individuals is treated as active antibodies. According to the degree of crowdedness, the active antibodies can clone, recombine and hyper mutate through the selection of a nondominated domain. NNIA has an obvious advantage in the high-dimensional multi-objective optimization problem because it pays more attention to the region with a low degree of crowdedness. Besides, NNIA is a multi-objective optimization algorithm on the basis of the Pareto optimal solution.

Figure 11 shows the flow chart of NNIA, and the main procedures of optimization are as follows:

(1) Initialization

The primary antibody group (B_0), dominated antibody group, activity antibody group and clone antibody group are generated in this procedure, where the size of the primary antibody group is n_D.

(2) Update dominant groups

The dominant antibodies (B_t) are recognized in this procedure. All dominant antibodies are copied to form the temporary dominant antibody group (DT_{t+1}).

(3) Select based on nondominated neighbor

If DT_{t+1} is not more than n_D, DT_{t+1} is set as D_{t+1}. Otherwise, the crowding distance between all individuals in the DT_{t+1} is calculated to arrange individuals in descending order. The top-n_D individuals in the first group form D_{t+1} according to the crowding distance in descending order. If D_t is not more than n_A, A_t is set as D_t. Otherwise, the top-n_D individuals in the first group form A_t according to the crowding distance in descending order.

(4) Proportional clone

Clone group (C_t) is obtained through applying the proportional clone on A_t.

(5) Recombination and hypermutation

Clone group (C_t) is reorganized and hyper mutated. C is set as a new clone group (C_t) and proceeds to step 2.

(6) End

If t is more than $G_{\max}$, D_{t+1} is exported as the result of the multi-objective optimization algorithm. Otherwise, t is set as $t + 1$.

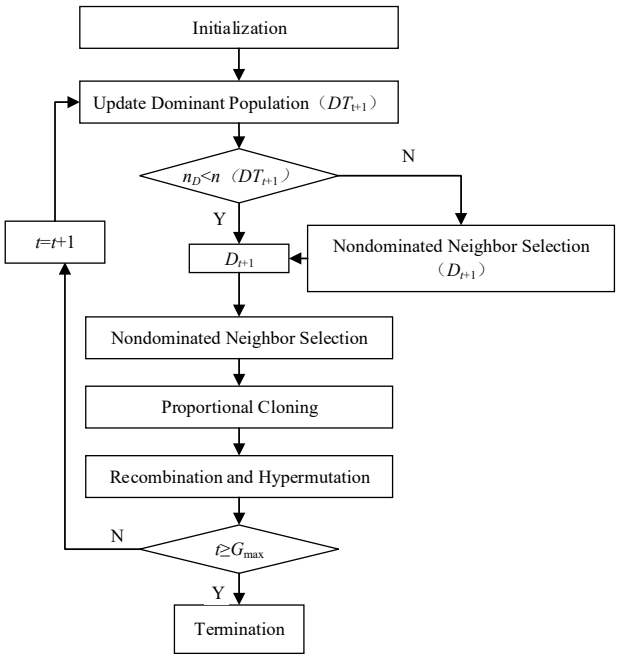

Figure 11. The flow chart of NNIA.

According to the experience and configuration of the WEDM machine tool, the multi-objective optimization model is developed to obtain high machining efficiency and good surface quality, as shown in Equation (4).

$$\begin{gathered} \text{Max } MRR(T_{on}, T_{off}, SV, WF, WT) \\ \text{Min } SR(T_{on}, T_{off}, SV, WF, WT) \\ \begin{cases} 250 \leq T_{on} \leq 450 \\ 8 \leq T_{off} \leq 12 \\ 40 \leq SV \leq 50 \\ 8 \leq WF \leq 12 \\ 10 \leq WT \leq 14 \end{cases} \end{gathered} \tag{4}$$

4.2. Optimization Results

Figure 12 shows the partial solution set of the multi-objective optimization algorithm. Table 7 shows the partial Pareto optimal solution of *MRR* and *SR*. In the Pareto optimal

solution, *MRR* is found to be negatively correlated with *SR*. This means that there is no process parameter combination that can simultaneously obtain the highest *MRR* and lowest *SR*. Besides, when a single objective is taken into account, the maximum *MRR* and the minimum *SR* can reach 0.501 mm^2/s and 4.32 μm, respectively. Moreover, this Pareto optimal solution of *MRR* and *SR* can be utilized for selecting process parameters in different machining conditions.

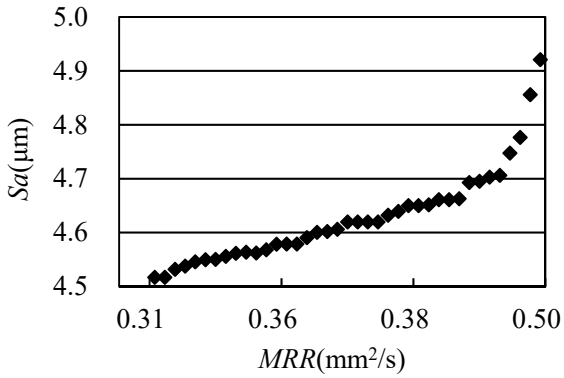

Figure 12. The partial Pareto optimal solution of *MRR* and *SR*.

Table 7. Partial solution set of multi-objective optimization algorithm.

No.	T_{on} (ns)	T_{off} (μs)	*SV* (V)	*WF* (mm/s)	*WT* (N)	*MRR* (mm^2/s)	*SR* (μm)
1	271.503	9.037	48.087	10.120	10.375	0.265	4.432
2	293.039	8.878	46.924	9.782	10.107	0.300	4.473
3	303.687	8.902	46.584	9.682	10.035	0.313	4.497
4	308.969	9.061	45.788	10.124	10.000	0.325	4.517
5	308.969	9.061	45.788	10.124	10.000	0.325	4.517
6	310.998	8.809	45.450	10.036	10.028	0.333	4.532
7	295.618	9.320	43.293	10.054	10.116	0.340	4.538
8	311.623	8.928	44.688	9.789	10.000	0.342	4.546
9	315.157	8.629	45.099	9.829	10.033	0.344	4.550
10	315.690	8.649	45.042	9.813	10.015	0.345	4.550
11	317.643	8.565	44.972	9.811	10.015	0.348	4.556
12	320.783	8.710	45.017	9.801	10.000	0.349	4.562
13	320.520	8.703	44.966	9.816	10.018	0.349	4.564
14	320.672	8.626	45.016	9.799	10.010	0.350	4.562
15	313.245	8.994	43.829	10.169	10.052	0.353	4.568
16	326.959	8.637	44.950	9.826	10.014	0.356	4.579
17	319.949	8.593	44.392	9.892	10.092	0.357	4.579
18	319.949	8.593	44.392	9.892	10.092	0.357	4.579
19	330.657	8.633	44.827	9.804	10.020	0.361	4.591
20	335.113	8.751	44.907	9.781	10.008	0.363	4.601
21	324.903	9.258	43.583	10.096	10.057	0.364	4.602
22	340.553	8.626	45.175	9.803	10.000	0.366	4.606
23	345.196	8.826	45.208	9.803	10.000	0.368	4.620
24	345.196	8.826	45.208	9.803	10.000	0.368	4.620
25	334.903	9.164	43.983	10.296	10.028	0.368	4.620
26	334.903	9.164	43.983	10.296	10.028	0.368	4.620
27	343.686	8.265	45.408	10.111	10.272	0.370	4.632
28	349.621	8.904	44.750	10.081	10.000	0.376	4.640
29	353.985	9.032	44.959	9.742	10.000	0.377	4.650
30	353.985	9.032	44.959	9.742	10.000	0.377	4.650
31	347.267	9.367	43.899	10.134	10.012	0.379	4.652
32	357.445	9.079	44.922	9.689	10.000	0.380	4.661
33	357.445	9.079	44.922	9.689	10.000	0.380	4.661
34	359.978	9.020	45.061	9.821	10.000	0.381	4.663
35	369.428	9.133	44.810	10.144	10.000	0.391	4.693
36	370.827	8.977	44.749	9.950	10.000	0.395	4.695

Table 7. *Cont.*

No.	T_{on} (ns)	T_{off} (μs)	*SV* (V)	*WF* (mm/s)	*WT* (N)	*MRR* (mm^2/s)	*SR* (μm)
37	362.786	9.330	43.388	10.522	10.037	0.399	4.703
38	370.103	8.954	43.861	10.475	10.000	0.403	4.706
39	384.842	9.333	43.913	10.422	10.000	0.413	4.748
40	394.872	8.616	44.836	9.349	10.214	0.421	4.777
41	382.195	8.022	44.406	9.470	11.378	0.444	4.856
42	426.537	10.934	41.986	10.369	10.366	0.501	4.921

Comparing Tables 4 and 7, the comparative results of *MRR* and *SR* under the optimized and original process parameters can be obtained, as shown in Table 8. It can be found that for No. 1–2 in Table 4, *MRR* with the original process parameters is almost the same as that using the optimized process parameters, and *SR* can be reduced by nearly 6.4%. For No. 3–4 in Table 4, *SR* with the original process parameters is almost the same as that using the optimized process parameters, and *MRR* can be increased by 28–34%. This proves that the proposed multi-objective optimization method of NNIA can effectively improve the machining characteristics of the SiCp/Al composite in WEDM.

Table 8. The comparative results of *MRR* and *SR* under optimized and original process parameters.

No.	Original		Optimized		Improvement
	MRR (mm^2/s)	*SR* (μm)	*MRR* (mm^2/s)	*SR* (μm)	
1	0.296	4.78	0.3	4.473	−6.4% *SR*
2	0.354	4.88	0.353	4.568	−6.3% *SR*
3	0.308	4.69	0.395	4.695	+28% *MRR*
4	0.315	4.77	0.421	4.777	+34% *MRR*

4.3. Verified Experiment

To evaluate the reliability and precision of the Pareto optimal solution, a set of verified experiments is conducted. Table 9 shows the comparison of verified experimental data and predicted data. The relative error between the verified experimental data and predicted data in the Pareto optimal solution ranges from 3.14% to 10.61%. This means that the Pareto optimal solution with NNIA has high reliability and precision.

Table 9. The comparison of verified experimental data and predicted data.

No.	Process Parameters					*Ra*			*MRR*		
	T_{on} (ns)	T_{off} (μs)	*SV* (V)	*WF* (mm^2/s)	*WT* (N)	Exp.	Pre.	Re. (%)	Exp.	Pre.	Re. (%)
1	300	9	47	10	10	4.75	4.49	5.79	0.341	0.313	8.95
2	350	9	45	10	10	4.9	4.65	5.38	0.417	0.377	10.61
3	400	9	45	9	10	4.92	4.77	3.14	0.449	0.421	6.65

Exp.: Verified experimental data, Pre.: Predicted data, Re.: Relative error.

5. Conclusions

(1) The methods of material removal of the SiCp/Al composite include sublimating, decomposing and particle shedding. The shedding pit is the primary cause of high surface roughness on the machined surface.

(2) The material removal rate (*MRR*) is found to increase with an increasing pulse-on time (from 0.265 mm^2/s to 0.465 mm^2/s), which first increases and then decreases with an increasing pulse-off time (from 0.374 mm^2/s to 0.404 mm^2/s, and to 0.315 mm^2/s), servo voltage (from 0.408 mm^2/s to 0.430 mm^2/s, and to 0.308 mm^2/s), wire feed (from 0.364 mm^2/s to 0.404 mm^2/s, and to 0.351 mm^2/s) and wire tension (from 0.348 mm^2/s

to 0.404 mm^2/s, and to 0.364 mm^2/s). The pulse-on time (the maximum difference up to 0.74 μm) and servo voltage (the maximum difference up to 0.45 μm) are the dominant factors for surface roughness (*SR*).

(3) The proposed multi-objective optimization method of NNIA can increase the machining speed and reduce the surface roughness of the SiCp/Al composite in WEDM. Specifically, NNIA can increase *MRR* by 34% and reduce *SR* by 6.4%.

The Pareto optimal solution by NNIA is proved to possess high reliability and precision, which can be utilized for selecting process parameters in different machining conditions. In future work, we will adopt more direct methods to reveal the machining mechanism of SiCp/Al in EDM/WEDM, such as thermal FEM, molecular dynamics simulation and high-speed observation.

Author Contributions: H.Y.: Conceptualization, funding acquisition, formal analysis, methodology, investigation, writing. B.D.K.: Data curation, investigation, resources, formal analysis, writing. H.Z.: Data curation, investigation. C.W.: Data curation. Z.C.: Funding acquisition, investigation, methodology, validation. All authors have read and agreed to the published version of the manuscript.

Funding: This research is supported by the National Natural Science Foundation of China (Grant No. 51805552), the Natural Science Foundation of Hunan Province, China (Grant No.2020JJ5721), and the Fundamental Research Funds for the Central Universities of Central South University (grant no. 512191021).

Institutional Review Board Statement: Not applicable.

Informed Consent Statement: Not applicable.

Data Availability Statement: The study did not report any data.

Conflicts of Interest: The authors declare no conflict of interest.

References

1. Moreno, M.F.; Oliver, C.J.R.G. Compression creep of PM aluminum matrix composites reinforced with SiC short fibres. *Mater. Sci. Eng. A-Struct. Mater. Prop. Microstruct. Process.* **2006**, *418*, 172–181. [CrossRef]
2. Sahin, Y. Wear behaviour of aluminium alloy and its composites reinforced by SiC particles using statistical analysis. *Mater. Des.* **2003**, *24*, 95–103. [CrossRef]
3. Dandekar, C.R.; Shin, Y.C. Modeling of machining of composite materials: A review. *Int. J. Mach. Tools Manuf.* **2012**, *57*, 102–121. [CrossRef]
4. Wang, J.F.; Fan, X.L.; Cao, Y.W.; Chu, K.Y.; Wang, K. Experimentation investigations of surface roughness in High-speed turning of SiCp/Al composites. *Chin. J. Mech. Eng.* **2017**, *15*, 62–66.
5. Yan, H.Z.; Kabongo, D.B.; Yan, Z.J.; Han, F.L.; Chen, Z. Sustainable production of high-uniformity workpiece surface quality in wire electrical discharge machining by fabricating surface microstructure on wire electrode. *J. Clean. Prod.* **2020**, *259*, 120881. [CrossRef]
6. Yan, H.Z.; Kabongo, D.B.; Chen, Z.; Yan, Z.J.; Zhou, H.B.; Han, F.L. Attainment of high corner accuracy for thin-walled sharp-corner part by WEDM based on magnetic field-assisted method and parameter optimization. *Int. J. Adv. Manuf. Technol.* **2020**, *106*, 4845–4857. [CrossRef]
7. Chen, Z.; Yan, Z.J.; Yan, H.Z.; Han, F.L. Improvement of the machining characteristics in WEDM based on specific discharge energy and magnetic field–assisted method. *Int. J. Adv. Manuf. Technol.* **2019**, *103*, 3033–3044. [CrossRef]
8. Chen, Z. Study on the white layer in wire electrical discharge trim cutting of bearing steel GCr15. *Int. J. Adv. Manuf. Technol.* **2019**, *102*, 2375–2386. [CrossRef]
9. Shen, D.; Ming, W.; Ren, X.; Xie, Z.; Zhang, Y.; Liu, X. A Cuckoo Search Algorithm Using Improved Beta Distributing and Its Application in the Process of EDM. *Crystals* **2021**, *11*, 916. [CrossRef]
10. Balasubramaniam, V.; Baskar, N.; Narayanan, C.S. Effect of process parameters on the electrical discharge machining of aluminum metal matrix composites through a response surface methodology approach. *Sci. Eng. Compos. Mater.* **2016**, *23*, 145–154. [CrossRef]
11. Gu, L.; Chen, J.P.; Xu, H.; Zhao, W.S. Blasting erosion arc machining of 20 vol.% SiC/Al metal matrix composites. *Int. J. Adv. Manuf. Technol.* **2016**, *87*, 2775–2784. [CrossRef]
12. Dey, A.; Debnath, S.; Pandey, K.M. Optimization of electrical discharge machining process parameters for Al6061/cenosphere composite using grey-based hybrid approach. *Trans. Nonferrous Met. Soc. China* **2017**, *27*, 998–1010. [CrossRef]
13. Daneshmand, S.; Masoudi, B. Investigation and optimization of the electro-discharge machining parameters of 2024 aluminum alloy and Al/7.5% Al2O3 particulate-reinforced metal matrix composite. *Sci. Eng. Compos. Mater.* **2018**, *25*, 159–172. [CrossRef]

14. Shelvaraj, S.G.; Naveen, S.A. Optimization of EDM Parameters for Al-TiC Composites Prepared through Powder Metallurgy Route. *Mechanika* **2018**, *24*, 135–142.
15. Singh, B.; Kumar, J.; Kumar, S. Investigation of the Tool Wear Rate in Tungsten Powder-Mixed Electric Discharge Machining of AA6061/10%SiCp Composite. *Mater. Manuf. Process.* **2016**, *31*, 456–466. [CrossRef]
16. Pramanik, A. Electrical Discharge Machining of MMCs Reinforced with Very Small Particles. *Mater. Manuf. Process.* **2016**, *31*, 397–404. [CrossRef]
17. Kumar, N.M.; Kumaran, S.S.; Kumaraswamidhas, L.A. High temperature investigation on EDM process of Al 2618 alloy reinforced with Si3N4, ALN and ZrB2 in-situ composites. *J. Alloys Compd.* **2016**, *663*, 755–768. [CrossRef]
18. Bains, P.S.; Sidhu, S.S.; Payal, H.S. Magnetic Field Assisted EDM: New Horizons for Improved Surface Properties. *Silicon* **2018**, *10*, 1275–1282. [CrossRef]
19. Kumar, T.T.S.; Subramanian, R.; Velmurugan, C.; Vinoth, K.S. Experimental investigations on wire electrical discharge machining characteristics of aluminum hybrid composites. *Indian J. Eng. Mater. Sci.* **2018**, *25*, 281–290.
20. Uthayakumar, M.; Babu, K.V.; Kumaran, S.T.; Kumar, S.S.; Jappes, J.T.W.; Rajan, T.P.D. Study on the machining of Al–SiC functionally graded metal matrix composite using die-sinking EDM. *Part Sci. Technol.* **2019**, *37*, 103–109. [CrossRef]
21. Senthilkumar, T.S.; Muralikannan, R. Role of TiC and h-BN particles on morphological characterization and surface effects of Al 4032 hybrid composites using EDM process. *J. Mech. Sci. Technol.* **2019**, *33*, 4255–4264. [CrossRef]
22. Paswan, K.; Pramanik, A.; Chattopadhyaya, S.; Basak, A.K. A novel approach towards sustainable electrical discharge machining of metal matrix composites (MMCs). *Int. J. Adv. Manuf. Technol.* **2020**, *106*, 1477–1486. [CrossRef]
23. Devi, M.B.; Sameer, M.D.; Birru, A.K. EDM machining characteristics of bamboo leaf ash and alumina reinforced aluminum hybrid metal matrix composite using Multi-response optimization by grey relational analysis. *Mater. Res. Express* **2021**, *8*, 016518. [CrossRef]
24. Sokołowski, D.; Kamiński, M. Probabilistic homogenization of hyper-elastic particulate composites with random interface. *Compos. Struct.* **2020**, *241*, 112118. [CrossRef]
25. Chen, Z.; Zhou, H.B.; Yan, Z.J.; Han, F.L.; Yan, H.Z. Machining characteristics of 65 vol.% SiCp/Al composite in micro-WEDM. *Ceram Int.* **2020**, *47*, 13533–13543. [CrossRef]
26. Chen, Z.; Zhang, G.J.; Han, F.L.; Zhang, Y.M.; Rong, Y.M. Determination of the optimal servo feed speed by thermal model during multi-pulse discharge process of WEDM. *Int. J. Mech. Sci.* **2018**, *142*, 359–369. [CrossRef]
27. Pan, H.W.; Liu, Z.D.; Li, C.R.; Zhang, Y.Q.; Qiu, M.B. Enhanced debris expelling in high-speed wire electrical discharge machining. *Int. J. Adv. Manuf. Technol.* **2017**, *93*, 2913–2920. [CrossRef]
28. Perumal, A.; Azhagurajan, A.; Baskaran, S.; Prithivirajan, R.; Narayansamy, P. Statistical evaluation and performance analysis of electrical discharge machining (EDM) characteristics of hard Ti-6Al-2Sn-4Zr-2Mo alloy. *Mater. Res. Express* **2019**, *6*, 056552. [CrossRef]
29. Mouliprasanth, B.; Hariharan, P. An Experimental Study and Analysis of Different Dielectrics in Electrical Discharge Machining of Al 6063 Alloy. *J. Polym. Mater.* **2019**, *36*, 351–369. [CrossRef]
30. Kong, L.L.; Liu, Z.D.; Qiu, M.B.; Wang, W.Z.; Han, Y.X.; Bai, S.K. Machining characteristics of submersed gas-flushing electrical discharge machining of Ti6Al4V alloy. *J. Manuf. Process.* **2019**, *41*, 188–196. [CrossRef]
31. Das, S.; Joshi, S.N. Estimation of wire strength based on residual stresses induced during wire electric discharge machining. *J. Manuf. Process.* **2020**, *53*, 406–419. [CrossRef]
32. Ming, W.Y.; Jia, H.J.; Zhang, H.M.; Zhang, Z.; Liu, K.; Du, J.G.; Shen, F.; Zhang, G.J. A comprehensive review of electric discharge machining of advanced ceramics. *Ceram Int.* **2020**, *46*, 21813–21838. [CrossRef]
33. Sergey, N.G.; Khaled, H.; Marina, A.V.; Anna, A.O.; Sergey, V.F. Electrical discharge machining of oxide and nitride ceramics: A review. *Mater. Design* **2021**, *209*, 109965.